A highly stabilized Ni-rich NCA cathode for high-energy lithium-ion batteries

Hoon-Hee Ryu[1], Nam-Yung Park[1], Jeong Hyun Seo[2], Young-Sang Yu[3], Monika Sharma[4], Robert Mücke[4], Payam Kaghazchi[4,*], Chong S. Yoon[2,*] Yang-Kook Sun[1,*]

[1]Department of Energy Engineering, Hanyang University, Seoul 04763, South Korea
[2]Department of Materials Science and Engineering, Hanyang University, Seoul 04763, South Korea
[3]Advanced Light Source, Lawrence Berkeley National Laboratory, Berkeley, CA 94720, USA
[4]Forschungszentrum Jülich GmbH, Institute of Energy and Climate Research, Materials Synthesis and Processing (IEK-1), 52425, Jülich, Germany

*** Corresponding authors.**
***E-mail addresses*: Kaghazchi, P. (payamk@zedat.fu-berlin.de) Yoon, C.S. (csyoon@hanyang.ac.kr), Sun, Y.-K. (yksun@hanyang.ac.kr)**

Abstract

In this study, we have demonstrated that boron doping of Ni-rich $Li[Ni_xCo_yAl_{1-x-y}]O_2$ dramatically alters the microstructure of the material. $Li[Ni_{0.885}Co_{0.1}Al_{0.015}]O_2$ is composed of large equiaxed primary particles, whereas a boron-doped $Li[Ni_{0.878}Co_{0.097}Al_{0.015}B_{0.01}]O_2$ cathode consists of elongated particles that are highly oriented to produce a strong, crystallographic texture. Boron reduces the surface energy of the (003) planes, resulting in a preferential growth mode that maximizes the (003) facet. This microstructure modification greatly improves the cycling stability; the $Li[Ni_{0.878}Co_{0.097}Al_{0.015}B_{0.01}]O_2$ cathode maintains a remarkable 83% of the initial capacity after 1000 cycles even when it is cycled at 100% depth of discharge. By contrast, the $Li[Ni_{0.885}Co_{0.1}Al_{0.015}]O_2$ cathode retains only 49% of its initial capacity. The superior cycling stability clearly indicates the importance of the particle microstructure (i.e., particle size, particle shape, and crystallographic orientation) in mitigating the abrupt internal strain caused by phase transitions in the deeply charged state, which occurs in all Ni-rich layered cathodes. Microstructure engineering by surface energy modification, when combined with protective coatings and composition modification, may provide a long-sought method of harnessing the high capacity of Ni-rich layered cathodes without sacrificing the cycling stability.

Keywords: Ni-rich NCA cathodes, Microstructural modifications, Boron doping, Microcracks

1. Introduction

With increasing pressure to reduce carbon emissions and dependence on fossil fuels, the public is increasingly aware of the need for widespread adoption of electric vehicles (EVs) but is still slow to embrace EVs, mainly because of their inadequate battery performance and high cost. EVs appeared in the 1890s, before internal combustion engine vehicles (ICEVs), but were gradually displaced by ICEVs owing to their limited driving range and relatively high cost [1–3]. Since then, the cost of batteries has decreased dramatically with market expansion and advances in battery technology; it is expected to decrease even further in the future. However, an important technical challenge facing today's EV batteries, especially Li-ion batteries (LIBs), which provide power for the current fleet of EVs, is the driving range per charge [4]. The driving range of EVs depends strongly on the reversible capacity of the cathode in the LIB. Hence, recent research on LIBs has concentrated mainly on identifying and optimizing high-capacity cathodes; the primary candidate materials are Ni-rich layered $LiMO_2$ (M = Ni, Co, Mn, and/or Al). In the last decade, the Ni composition of these cathodes has increased from 33% to more than 90%; consequently, these Ni-rich $LiMO_2$ cathodes deliver a reversible capacity close to the theoretical value of ~275 mAh g^{-1} [5–8]: 229 mAh g^{-1} for $Li[Ni_{0.9}Co_{0.05}Mn_{0.05}]O_2$, 238 mAh g^{-1} for $Li[Ni_{0.95}Co_{0.025}Mn_{0.025}]O_2$, and 247 mAh g^{-1} for $LiNiO_2$. Increasing the nickel content not only increases the energy density of the LIBs but also decreases the battery cost by reducing the use of expensive Co. However, the high capacity of Ni-rich $LiMO_2$ is accompanied by poor cycling performance stemming from microcracks that form in the cathode particles in the deeply charged state [7–12]. When these microcracks propagate to the particle surface, they facilitate degradation of the exposed internal surfaces through parasitic reactions with the infiltrated electrolyte. To minimize such microcracking, cylindrical LIBs based on Ni-rich lithium nickel cobalt aluminum oxide (NCA) cathodes, which are currently deployed in EVs such as Tesla models S, X, and 3, have to be cycled with a limited depth of discharge (DOD) of 60% [13]. Limiting the DOD range adds dead weight to the battery and significantly reduces the energy density, thus increasing the cost of EVs.

To improve the cycling stability without limiting the DOD, it is necessary to suppress the formation of microcracks, which nucleate from the abrupt lattice contraction caused by the

H2 → H3 phase transition. Ni-rich $LiMO_2$ cathodes have been compositionally modified to protract this phase transition and reduce its abruptness [11,12,14,15]. For example, the abrupt H2 → H3 phase transition of the compositionally partitioned $Li[Ni_{0.9}Co_{0.05}Mn_{0.05}]O_2$ cathode, labeled as CSG90, was alleviated due to the gradual spatial distribution of Ni ions in the outer shell layer. The configuration of an encapsulating shell effectively reduces the level of imposed stress on the whole particle during the electrochemical reaction.[11] Alternatively, both the external surfaces and internal interparticle boundaries have been passivated to protect the surface from electrolyte attack. Yan et al. reported that surface and grain boundaries coating with Li_3PO_4 effectively prevented the electrolyte penetration and following the attack of the internal surface [16]. These approaches have been somewhat successful; however, it is questionable whether they could be extended to layered $LiMO_2$ cathodes with a Ni fraction exceeding 0.9, which are needed to meet the driving range requirement for next-generation EVs. A holistic approach, rather than exclusive reliance on chemical modifications, is needed to address microcrack formation, which becomes increasingly severe with increasing Ni fraction. Although intrinsic lattice volume changes are unavoidable during electrochemical reactions, the structural integrity of Ni-rich $LiMO_2$ cathodes can be preserved by engineering the microstructure of cathode particles such that the strain distribution is delocalized. The internal strain, which is generated by abrupt collapse of the oxygen–ion framework caused by excessive removal of Li ions from the Li layer, occurs mainly in the *c* direction; hence, primary particles with strong crystallographic texture can provide a uniform strain distribution and suppress the local stress concentrations that often lead to microcrack nucleation. Such crystallographic texture, in which the *a* axis of each primary particle is aligned along the radial direction, will allow a cathode particle to contract and expand uniformly during cycling and minimize the local strain build-up. For example, in a compositionally partitioned Ni-rich $Li[Ni_{0.9}Co_{0.05}Mn_{0.05}]O_2$ cathode, the radially aligned primary particles improved the cycling stability by suppressing microcrack formation [11]. The concept of using spatial confinement and primary particles with radial crystallographic texture to negate the anisotropic strain during cycling and inhibit the formation of microcracks was extended, and boron doping of a nickel cobalt manganese oxide (NCM) cathode was shown to modify the surface energy, resulting in the development of radial crystallographic texture

in $Li[Ni_{0.9}Co_{0.05}Mn_{0.05}]O_2$ without concentration gradients and improving the cathode cycling performance [17]. In this study, simply introducing boron into a Ni-rich NCA cathode dramatically alters the morphology and orientation of the primary particles; consequently, the $Li[Ni_{0.885}Co_{0.1}Al_{0.015}]O_2$ cathode exhibits strong radial crystallographic structure that mitigates the intrinsic poor cycling performance of the cathode at 100% DOD. This result clearly demonstrates that microstructure engineering by tailoring the surface energies can be used to effectively dissipate the internal strain resulting from the detrimental phase transition. To highlight the dramatic microstructure change caused by boron doping, B-doped $Li[Ni_{0.878}Co_{0.097}Al_{0.015}B_{0.01}]O_2$ (B-NCA88) and pristine $Li[Ni_{0.885}Co_{0.1}Al_{0.015}]O_2$ (P-NCA89) cathodes are extensively investigated by comparing their electrochemical properties, microcracking behavior, and structural stability.

2. Materials and Methods

2.1 Synthesis of cathode materials

Spherical $[Ni_{0.9}Co_{0.10}](OH)_2$ precursor was synthesized by a co-precipitation method. More detail is provided in previous papers [18]. To synthesize P-NCA89, the precursor $[Ni_{0.9}Co_{0.10}](OH)_2$ was mixed with $LiOH{\cdot}H_2O$ (Sigma-Aldrich) and $Al(OH)_3$ (Sigma-Aldrich) (Li:(Ni+Co+Al) = 1.01:1, Al/(Ni+Co+Al) = 0.015 in molar ratio) and calcined at 730°C for 10 h under flowing O_2. Similarly, to synthesize B-NCA88, the hydroxide precursor was mixed with $LiOH{\cdot}H_2O$ Sigma-Aldrich), $Al(OH)_3$ (Sigma-Aldrich) and 0.5 mol% of B_2O_3 (Alfa Aesar)for boron doping, and the mixture was calcined at the same condition as P-NCA89.

2.2 Analytical Techniques

2.2.1 Material characterization and electrochemical test

The chemical composition of materials was identified by inductively coupled plasma spectroscopy (iCAP 7000 SERIES, Thermo Fisher Scientific). Powder XRD measurements were carried out using synchrotron radiation on the 9B-HRPD beamline (λ = 1.51670 Å) at Pohang Accelerator Laboratory (PAL) in Pohang, Korea. The XRD profiles for both cathodes were

obtained in the 2θ range 10−130° at a 0.01° step size. In situ XRD measurements were performed with the incident beam of 0.65303 Å at the 6D UNIST beamline at PAL in Pohang, Korea. Modified 2032 coin-type half-cells having a 3 mm-diameter hole at its center were used for in situ XRD measurement. The holes on both sides served as the X-ray beam path were sealed with Imide tape. The sample-to-detector distance were calibrated using a CeO_2 standard. For electrochemical reaction during in situ XRD measurement, a loading of the electrodes was about 12 mg cm^{-2} containing 90% of the active material and the applied specific current was 40 mA g^{-1}. The XRD profile was recorded every 3.5 min with a 2D detector (Rayonix MX225-HS). The electrodes were cut using a cross-sectional polisher (CP, IB-19520CCP, JEOL). For the TEM samples, a particle was cut into less than 100 nm thick thin foil using a focused ion beam (FIB, JEM 2100F, JEOL) and loaded onto a Mo grid. For electrochemical tests, details are previously described [11,12].

The positive electrodes were fabricated by casting a slurry mixed with the active materials, carbon black and poly(vinylidene fluoride) (by weight ratio of 90:5.5:4.5 for half-cell test and 94:3:3 for full-cell test). The slurry was coated on Al foil and roll-pressed, and vacuum dried. The active material loading level was 4–5 mg cm^{-2} for half-cell electrode (14 mm in diameter) and 9–10 mg cm^{-2} for full-cell electrode (30 mm x 50 mm size). The electrolyte solution was 1.2 mol L^{-1} $LiPF_6$ in ethylene carbonate-ethyl methyl carbonate by 3:7 volume ratio with 2 wt% vinylene carbonate. The half-cells were tested between 2.7 and 4.3 V voltage window. A full-cell capacity balance was in the range of 1.15–1.2 and cycled between 3.0 and 4.2 V by applying a constant 1C specific current of 200 mA g^{-1} at 25℃.

2.2.2 Density functional theory (DFT) calculations

Spin-polarized DFT calculations were performed using the projector-augmented plane-wave method implemented in the Vienna Ab Initio Simulation Package. We used the SCAN functional and an energy cutoff of 500 eV. We modeled P-NCA89 and B-NCA88 using $LiNi_{0.92}Co_{0.04}Al_{0.04}O_2$ and $LiB_{0.02}Ni_{0.9}Co_{0.04}Al_{0.04}O_2$ formula units, respectively, with $R\bar{3}m$ symmetry. We used a B concentration of 2% with respect to the Ni cations ($LiB_{0.02}Ni_{0.9}Co_{0.04}Al_{0.04}O_2$) to model B-NCA88. Owing to their small size, B ions were considered

to occupy Ni sites. We used a hexagonal bulk unit cell to model all the surfaces except the pristine and B-doped Li-rich nonstoichiometric (003) surfaces, which were modeled using a rectangular bulk unit cell. The optimized unit cell parameters and applied *k*-point meshes for the pristine bulk $LiNi_{0.92}Co_{0.04}Al_{0.04}O_2$ calculations were *a* = 11.314 Å, *b* = 11.593 Å, *c* = 14.052 Å, $\alpha = \beta = 90^{o}, \gamma = 120^{\circ}$, 2 × 2 × 2 for the hexagonal cell and *a* = 22.838 Å, *b* = 4.937 Å, *c* = 14.041 Å, $\alpha = \beta = \gamma = 90^{o}$, 1× 5 × 2 for the rectangular cell. The calculated unit cell parameters and *k*-point meshes for the corresponding B-doped bulks were *a* = 11.301 Å, *b* = 11.622 Å, *c* = 14.048 Å, $\alpha = \beta = 90^{o}, \gamma = 120^{\circ}$, 2 × 2 × 2 and *a* = 22.804 Å, *b* = 4.937 Å, *c* = 14.043 Å, $\alpha = \beta = \gamma = 90^{o}$, 1 × 5 × 2. To model the surfaces, we used the supercells that were used to model the bulk structures and considered eight-, five-, five-, and five-layer slabs for the (003), $(01\bar{2})$, (014), and (100) planes, respectively; we also introduced a vacuum space of at least 12 Å between slabs.

2.2.3 Finite element simulation

To compare the stresses inside the particles of the P-NCA89 and B-NCA88 cathodes, we manually redrew their microstructures from the SEM images using AutoCAD (Autodesk Inc., San Rafael, CA, USA) and determined the aspect ratio and orientation of the primary crystals using ImageJ [19]. The secondary particle of P-NCA89 consisted of 390 crystals, whereas the secondary B-NCA88 particle consisted of 754 crystals. To ensure high accuracy, a fine mesh with an element size of 20 nm was used for the elastic finite element analysis performed using ANSYS 2019R2 (Canonsburg, PA, USA). We used the anisotropic elastic constants C_{mn} *computed* by Yamakawa et al [20]. for $Li_{0.5}CoO_2$. To the best of our knowledge, the anisotropic elastic constants of NCA cathodes have not been reported to date. We also calculated the spatial stress $\sigma(x, y)$ using the isotropic stiffness data for NMC532 reported by Xu et al [21]. However, we found no significant difference between the $\sigma(x, y)$ values calculated using isotropic and anisotropic stiffness data (Fig. S1). To calculate $\sigma(x, y)$, the change in the anisotropic lattice parameters during charging, as measured by XRD as a function of the state of charge (Fig. S1), was used. The as-manufactured (uncharged, fully lithiated) particles were assumed to be in the stress-free state. No external forces were applied during the simulation.

2.2.4 Spectrally sensitive imaging by soft X-rays

Ni oxidation state maps were obtained using coherent scanning transmission X-ray microscopy (STXM) and the ptychographic imaging beamline (coherent scattering and microscopy, COSMIC) at the Advanced Light Source [22,23]. A coherent monochromatic X-ray beam was focused onto the sample by a Fresnel zone plate with an outer zone width of 45 nm and an order-sorting aperture. To ensure the transparency of the samples in the soft X-ray region, the secondary particles (diameter, ~10 μm) were sliced into thin sections (thickness, ~100 nm) along their central region by a focused ion beam (JEOL 2100F, JEOL). Two-dimensional raster scans of the transmitted and scattered X-ray were recorded by either an X-ray-sensitive PIN diode point detector (for STXM) or a two-dimensional fast charge-coupled device (CCD, for ptychography). STXM image spectra across the Ni *L*-edge (Fig. S2) afford spectral sensitivity, with the finest energy step of 0.25 eV near the absorption resonance features, from pixels with comparable resolution (a zone-plate-limited Raleigh resolution of 55 nm and a scan grid of 50 nm steps). The dwell time/pixel (3–5 ms) and slit sizes were chosen considering the required spectral resolution and radiation stability. For the ptychography study, the COSMIC beamline provided a resolution of three times the X-ray wavelength for 1 nm X-rays [24]. To expand the dynamic range of the detector, diffraction patterns in double exposure mode (combinations of 50 and 5 ms exposures at each scan point) were recorded directly on a custom fast-readout CCD without an attenuator. Two-dimensional diffraction patterns were obtained at the grid points (40 nm steps), where adjacent scan points overlapped (i.e., the X-ray beam was larger than the scan step). The patterns were reconstructed to provide both the complex transmission function of the sample and the illumination wavefield using 500 iterations of an implementation of the RAAR phase retrieval algorithm [25]. All the diffraction data processing, including ptychographic reconstruction and background retrieval [22], were performed using standard methods available in the SHARP-CAMERA software package with parallel computation (http://camera.lbl.gov).

2.2.5 Image processing

Because it is essential to eliminate image-to-image wobble in image spectra with subpixel resolution to obtain high-quality chemical information, an iterative registration method with

intensity-based automatic image alignment was adopted [26]. The image spectra were first roughly aligned with each preceding image using only a phase correlation algorithm with translations of pixel size. In the second alignment process, an intensity-based image registration algorithm determined the specific image transformation matrix that was applied to the moving image with bilinear interpolation, and the misaligned images (raw images) were brought into alignment with the reference image (average of the registered images). The iterative procedures were repeated until the aligned images were self-consistent. The registered image spectra through the sliced samples were converted to the pixel-by-pixel absorbance spectrum OD by taking the log ratio of the incident (I_0) and transmitted (I) intensities at each pixel, $\ln(I_0/I)$. To eliminate spectral distortions owing to the time gap between acquisition of the I_0 and I intensities, the incident beam intensity was simultaneously measured through an open area of the sample. To create the chemical composition maps, converted pixel-by-pixel XAS spectra from the STXM image spectra were fitted, where possible, with linear combinations (LCs) of standard spectra using a least-square method. Reference spectra for Ni^{2+} and Ni^{3+} were collected from $LiMn_{1.5}Ni_{0.5}O_4$ spinel and $LiNi_{0.8}Co_{0.15}Al_{0.05}O_2$ layered oxides, respectively (Fig. S3). Note that the use of the reference spectra is justified by comparison with the end-members calculated using non-negative matrix analysis (Fig. S4) [27]. Owing to the STXM resolution limits, the calculated end-members are represented by a mixture of Ni^{2+} and Ni^{3+} chemical species. The ratios of the chemical species from the pixel-by-pixel LC fitting results can be used to generate a color map (Fig. S2). For the ptychography study, the OD images at 852.75 and 855 eV were used to estimate the quantitative chemical information. Because the magnitude of the absorption at a certain energy is linearly proportional to the relative quantity of species with different Ni oxidation states, the chemical concentrations of Ni^{2+} and Ni^{3+} at each voxel can be calculated [26]. To maximize the chemical contrast, all the OD images were normalized by the OD image at the pre-edge (847 eV).

3. Results and Discussion

The chemical compositions of the synthesized B-NCA88 and P-NCA89 cathodes, determined by inductively coupled plasma spectrometry, are $Li[Ni_{0.878}Co_{0.097}Al_{0.015}B_{0.01}]O_2$ and $Li[Ni_{0.885}Co_{0.1}Al_{0.015}]O_2$, respectively. The X-ray diffraction (XRD) patterns in Fig. S5 reveal that both B-NCA88 and P-NCA89 have a hexagonal α-$NaFeO_2$-type structure belonging to the $R\bar{3}m$ space group without impurity phases. Both cathodes consist of nearly spherical particles with an average diameter of 10 μm (Fig. 1a,b). Each secondary particle consists of tightly packed nanosized primary particles. However, the morphology of the primary particles of the two cathodes is strikingly different, although both cathodes were produced using the same hydroxide precursor. The P-NCA89 cathode is composed of nearly equiaxed polygonal primary particles, which are typical of an NCA cathode[12,13]; by contrast, the B-NCA88 cathode is composed of needle-shaped primary particles smaller than those of P-NCA89. The elongated primary particles of B-NCA88 are ~500 nm long and ~100 nm wide. To better observe the dissimilarity in their interior microstructure, cross sections of both cathodes were examined using transmission electron microscopy (TEM). The bright-field scanning TEM image in Fig. 1c shows the relatively thick equiaxed primary particles of the P-NCA89 cathode. The particle size gradually decreases toward the center of the particle. In comparison, Fig. 1d, the primary particles of the B-NCA88 cathode have a long elongated shape with its length extending up to 3 μm (spanning nearly the entire hemisphere of the secondary particle). The introduction of boron into a Ni-rich NCA cathode dramatically modifies the particle morphology and spatially confines the elongated primary particles into a spoke-like structure. The reason for the modification is that boron doping accentuates the surface energy difference among the crystal planes. Boron doping favors the (003) planes, forcing the primary particles to grow into thin elongated shapes enclosed on the sides by the (003) planes while developing a strong crystallographic texture. Boron doping also reduces the surface energies of the $(01\bar{2})$ and (014) planes, which is discussed in the latter part; thus, the primary particles are capped by these crystal planes (Fig. 2a,b). Fig. 2c unequivocally shows the preference for the (003) facet. The *a* axis of the marked primary particle in Fig. 2c is skewed away from the particle center such that the radial texture is not maintained; however, because of the preference for the (003) facets, the sides of the marked particles develop zigzag surfaces so that the side surfaces are

terminated with (003) planes (Fig. 2d,e).

To verify the surface energy modification caused by boron doping, the stability of the P-NCA89 and B-NCA88 surfaces was compared by calculating the (003), $(01\bar{2})$, (014), and (100) surf ace energies of $LiNi_{0.92}Co_{0.04}Al_{0.04}O_2$ and $LiB_{0.02}Ni_{0.90}Co_{0.04}Al_{0.04}O_2$ using density function al theory (DFT). The surface energies were calculated as

$$\gamma = \frac{1}{2A}[E_{\text{surf}} - E_{\text{bulk}} + (N_{\text{Ni}} - N_{\text{Li}})\mu_{\text{Li}}] \quad (1)$$

Here, E_{surf} and E_{bulk} are the total energies of the surface and bulk structures, respectively. N_{Ni} and N_{Li} are the numbers of Ni and Li atoms on the surface. μ_{Li} is the chemical potential of Li, and A is the surface area of the slab. We modeled all the surfaces as nonpolar stoichiometric structures. Because the stoichiometric (003) surface is polar, we considered a nonpolar reconstructed structure to stabilize it. All the other surfaces are nonpolar when their unreconstructed stoichiometric compositions are considered. We also modeled nonpolar nonstoichiometric (003) and $(01\bar{2})$ surfaces with Li ion excesses and deficiencies in their topmost layers. The B dopant was initially located in the subsurface layers. Fig. 2f shows the surface energy plot $\gamma(\Delta\mu_{\text{Li}})$ of the pristine $LiNi_{0.92}Co_{0.04}Al_{0.04}O_2$ and B-doped $LiB_{0.02}Ni_{0.90}Co_{0.04}Al_{0.04}O_2$ surfaces. $\Delta\mu_{\text{Li}}$ was referenced to the total energy per atom of a metal Li reservoir. The low and high values of $\Delta\mu_{\text{Li}}$ represent Li-poor and -rich environments, respectively. Our calculations show that for $\Delta\mu_{\text{Li}} \leq -3.67$ eV, the Li-poor pristine $LiNi_{0.92}Co_{0.04}Al_{0.04}O_2$ (003) surface is indeed most stable, as it has the lowest value of γ. The stoichiometric pristine $LiNi_{0.92}Co_{0.04}Al_{0.04}O_2$ (014) and B-doped $LiB_{0.02}Ni_{0.90}Co_{0.04}Al_{0.04}O_2$ (014) surfaces are most favorable at -3.67 eV $\leq \Delta\mu_{\text{Li}} \leq -2.85$ eV. For -2.85 eV $\leq \Delta\mu_{\text{Li}}$, however, the non-stoichiometric Li-rich B-doped $LiB_{0.02}Ni_{0.90}Co_{0.04}Al_{0.04}O_2$ (003) surface, with a well-ordered layer having lithium boron oxide structure, becomes stable. Three O anions from the subsurface layer, together with the B dopant, form a curved Li_3BO_3 layer. The calculated average B–O bond length is 1.387 Å, which is similar to the value of 1.377 Å in the α-Li_3BO_3 phase observed by Stewner [28]. In addition, we find that the B-doped $(01\bar{2})$ surface is much more stable than the B-doped (100) surface. Thus, in comparison to the latter surface, the values of γ (for -2.85 eV $\leq \Delta\mu_{\text{Li}}$,) of the B-doped $(01\bar{2})$ surface are more similar to those

of the B-doped (003) and pristine and B-doped (014) surfaces. This result confirms the presence of the (003), (014), and $(01\bar{2})$ facets on the primary particles with B-doped $LiB_{0.02}Ni_{0.90}Co_{0.04}Al_{0.04}O_2$ microstructure.

The fundamental cell performance of the P-NCA89 and B-NCA88 cathodes was characterized using 2032 coin-type half-cells with a Li metal anode. A cycling test was performed between 2.7 and 4.3 V at a constant specific current of 18 mA g^{-1} (0.1C) for the first cycle and 90 mA g^{-1} (0.5C) for subsequent cycles. B-NCA88 delivered an initial discharge capacity of 222.4 mAh g^{-1} at 0.1C, whereas P-NCA89 produced a slightly higher discharge capacity of 224.8 mAh g^{-1} owing to its higher fraction of redox-active Ni (Fig. 3a). B-NCA88, however, exhibited remarkably improved cycling performance, with a capacity retention of 93.5% after 100 cycles, compared to 83.9% for P-NCA89 (Fig. 3b). The difference in cycling stability became more pronounced at an elevated temperature of 45 °C. The B-NCA88 cathode retained 88.7% of its initial capacity at 45 °C, whereas the capacity retention of the P-NCA89 cathode was only 74.4% (Fig. 3c). The cycling data demonstrate that boron doping greatly improves the cycling stability. To further demonstrate the enhanced cycling stability of the B-NCA88 cathode, the dQ/dV profiles are plotted in Fig. 3d,e. They were calculated by differentiating every 25th charge and discharge curve at 30 °C. Both cathodes, like Ni-enriched NCMs, exhibited four distinct redox peaks corresponding to the multiple phase transitions incurred by the cathodes during Li extraction/insertion. It is well known that the H2 → H3 phase transition at ~4.2 V is responsible for capacity fading, which is induced by the anisotropic lattice volume change [7–9]. The intensity of the H2/H3 redox peak of the P-NCA89 cathode gradually became polarized and decreased with cycling, indicating increasing irreversibility stemming from gradual formation of a NiO-like impurity layer along the exposed interior surface owing to electrolyte infiltration through microcracks [7,29]. By contrast, the intensity of the H2/H3 phase transition for the B-NCA88 cathode remained unchanged for up to 100 cycles.

To verify the cycling stability of the B-NCA88 cathode, cross sections of P-NCA89 and B-NCA88 cathode particles in different charged states (3.9, 4.0, 4.1, 4.2, and 4.3 V) and the subsequent discharged states (4.1 and 2.7 V) were observed using SEM (Fig. 4). The P-NCA89 cathode particle started to develop microcracks emanating from the particle center at 3.9 V, and the

microcracks progressively widened and propagated to the surface with increasing upper cutoff voltage. Above 4.1 V, at which the H2 → H3 phase transition occurs, the microcracks crossed the entire particle, and at 4.3 V they appeared to fracture the P-NCA89 secondary particle into several smaller fragments. During discharge, however, the microcracks were closed by compressive stress during the H3 → H2 phase transition, restoring the original microstructure. Despite the crack closure during discharge, these microcracks provide pathways that facilitate electrolyte penetration into the particle interior and thus expedite the surface degradation of the exposed interior primary particles by forming a NiO-like rocksalt surface layer [7,8,11,12]. The impurity layer, in turn, increases the impedance and weakens the mechanical integrity of the particle through repeated opening/closing of microcracks. By contrast, only a few microcracks nucleated at the center of the B-NCA88 particles, but they stopped before propagating to the surface, and the microcracks were barely visible even in the fully charged state. The SEM images in Fig. 4 clearly illustrate the structural stability resulting from boron doping.

To quantify the effect of boron doping on the lattice volume change during charging, in situ XRD experiments were conducted while both cathodes were charged to 4.5 V at a specific current of 40 mA g^{-1} (see Fig. S6a,b for the full XRD spectra). The charge curves obtained using the modified 2032 coin-type half-cell are nearly the same as those obtained using the normal 2032 coin-type half-cell (Fig. S6c,d). As shown in Fig. 5, the *a*-axis lattice parameters decreased monotonically as charging proceeded, whereas the *c*-axis lattice parameters initially expanded and began to contract beyond 4.0 V for both cathodes. Above 4.2 V, the *c*-axis lattice parameters abruptly decreased; the maximum *c*-axis contraction was 5.49% for P-NCA89 and 5.47% for B-NCA88. The calculated volume change for the unit cell was −7.4% for P-NCA89 and −7.6% for B-NCA88. The in situ XRD data suggest that boron doping did not affect the intrinsic structural changes associated with the multiple phase transitions in the cathode during delithiation. The characteristic abrupt volume contraction caused by the H2 → H3 phase transition appeared at nearly the same magnitude in the B-NCA88 cathode as in the P-NCA89 cathode. Hence, the microstructural modification, i.e., elongation of the primary particles with strong radial texturing, is likely responsible for the observed enhancement in

structural and cycling stability, underpinning the importance of the cathode microstructure.

To demonstrate the effect of the strong crystallographic texture on the structural stability during Li extraction, the stress distribution was calculated using a finite element simulation. To create a realistic model, the particle morphology and size distribution obtained from the corresponding cross-sectional TEM images (Fig. S1) were used for the calculation. In addition, the lattice contraction data from the in situ XRD experiment were used to model the strain development during Li extraction. The orientations of the *a* and *c* axes were randomly chosen for the pristine cathode, whereas in the B-doped cathode, only the primary pa rticles with an aspect ratio smaller than 2, e.g., the crystals in the core region, wer e assumed to be fully randomly oriented. The *a* axes of all the more-elongated crys tals were aligned parallel to their longitudinal direction, and most of them pointed r adially outward (Fig. 6a). The computed spatial stress distribution $\sigma(x, y)$ of the P-NCA89 and B-NCA88 cathodes during delithiation shows the significant advantage of th e B-NCA88 cathode over the undoped one (Fig. 6b,c). The magnitude of σ increases with delithiation up to *x* = 0.6 for both the P-NCA89 and B-NCA88 cathodes, as the difference between the crystallographic strain along the *a* (= *b*) and *c* axes, i.e., $\Delta a\ (= \Delta b)$ and Δc, reaches its maximum in this state of charge. The accumulated stress will cause crack growth or plastic deformation in most regions of the secondary particle. The stresses are significantly smaller for the doped B-NCA88 material in all cases where stresses are present. In particular, the shell region of the B-NCA88 particle remains rather stress-free, which ensures its integrity during electrochemical cycling. As the material properties of P-NCA89 and B-NCA88 are very similar [they have almost the same crystallographic strains (Fig. S1c,d) and the same stiffness], it becomes obvious that the greater stability of the latter is a result of the tailored microstructure of the doped particles, in particular the aligned crystallographic orientation in the shell region.

To assess the long-term cycling stability of the highly oriented B-NCA88 cathode, a pouch-type full-cell with a graphite anode was cycled between 3.0 and 4.2 V at 1C (180 mA g^{-1}). As shown in Fig. 7, the B-NCA88 cathode exhibited remarkable cycling stability, with a capacity retention of 83.4% after 1000 cycles, whereas the P-NCA89 cathode maintained only 49.0% of its initial

capacity (190.1 mAh g^{-1}). When cycled with a limited DOD of 60%, the P-NCA89 cathode exhibited greatly enhanced cycling performance, showing a capacity retention of 76.6%, which is similar to that of the B-NCA88 cathode cycled at DOD 100%; however, the P-NCA89 cathode delivered a much lower discharge capacity of 113.5 mAh g^{-1}, compared to 188 mAh g^{-1} for the B-NCA88 cathode. The enhancement of cycling stability by boron doping was also demonstrated in the NCA cathode of Ni 80% (Fig. S7). The full-cell performances demonstrate that the full utilization of B-NCA cathode's capacity largely increases the energy density of the battery to meet the driving range per charge of the threshold 300 miles, thus leading to a significant reduction of the battery cost. In addition, the high capacity retention of the B-NCA88 cathode is enough to guarantee a longer service life of battery. The superior cycling stability of the B-NCA88 cathode was further confirmed by in situ XRD measurement of the cathodes in pouch-type full-cells during the 1^{st} and 1000^{th} cycles, which was performed without disassembling the cells. The contour plots in the selected 2θ range containing the (003) reflection are shown in Fig. 8. During the first cycle, the (003) reflections of both cathodes shifted to a lower angle and then moved sharply to a higher angle owing to the H2 → H3 phase transition during charging. During discharge, the (003) reflection retraced the charging curve to produce a symmetric profile for both cathodes (Fig. 8a,b and Fig. S8a,b). After 1000 cycles at 1C, however, the contour plots differed dramatically. The (003) contour plot for the P-NCA89 cathode no longer showed the abrupt shifts corresponding to the H2 → H3 phase transition, whereas the B-NCA88 cathode maintained its initial (003) contour plot well even after repeated lattice contraction and expansion (Fig. 8c,d and Fig. S8c-f). The changes in the contour plots of the (003) reflection for the two cathodes agree well with the decay of the peak intensity of the H2 → H3 transition in the 1000^{th} dQ/dV profile (Fig. 8e,f). The H2 → H3 redox peak of the P-NCA89 cathode disappeared almost completely from its 1000^{th} dQ/dV profile, whereas the B-NCA88 cathode retained the distinct redox peaks arising from the multiple phase transitions even after 1000 cycles. After the in situ XRD measurement, the cycled cathodes were recovered to assess the microstructural damage in each cathode. As expected, the P-NCA89 particles in the fully discharged state after 1000 cycles were nearly pulverized into fragments (Fig. 8g). By contrast, the cycled B-NCA88 particles were free of microcracks anywhere in the particles, attesting to the material's superior reversibility (Fig.

8h).

To assess the extent of the surface damage during cycling, the Ni oxidation states were mapped by ptychographic soft X-ray microscopy combined with X-ray absorption spectroscopy (XAS) at the elliptically polarizing undulator beamline (7.0.1.2) at the Advanced Light Source, Lawrence Berkeley National Laboratory, Berkeley, CA (USA). Prolonged exposure of the internal surfaces to the electrolyte as a result of repeated opening and closing of microcracks accelerated the accumulation of a NiO-like rocksalt impurity layer. To explicitly observe the structural damage caused by electrolyte attack, the cross sections of the discharged cathodes after 100 cycles were examined by capturing optical density maps with high spectral (resolving power $E/\Delta E \leq 2500$) and spatial (~5 nm) sensitivity. Fig. 9 shows the XAS images [i.e., multiple optical density (OD) images obtained across the Ni L-edge, 845–880 eV] from the marked region in the bright-field scanning TEM images. The quantitative distributions of distinct chemical phases were mapped by comparing the image spectra pixel-by-pixel with reference spectra (see the supplementary data). In the chemical composition map (Fig. 9 and Fig. S2), the fitting results (chemical information) and averaged OD (morphological information) are indicated by color and transparency, respectively. Ni^{3+} and Ni^{2+} appear as red and green, respectively. A qualitative comparison of the spectra of the cathodes shows a marked difference in the intergranular degradation of the primary particles. In the P-NCA89 cathode, nearly all the interparticle boundaries of the primary particle were completely passivated by the Ni^{2+} phase. The distribution of the Ni^{3+} phase is not uniform but is depleted along the interparticle boundaries, indicating that the cathode was not fully discharged. On the other hand, although some regions suffered from surface degradation along the grain boundaries, the Ni^{3+} map confirmed that most primary particles were uniformly restored to their fully lithiated state, indicating the enhanced cycling stability of the B-NCA88 cathode.

4. Conclusion

A simple process of adding boron during lithiation of a Ni-rich NCA precursor dramatically altered the microstructure of a cathode. A P-NCA89 cathode without boron was composed of large equiaxed primary particles, whereas a boron-doped B-NCA88 cathode consisted of

elongated particles that were highly oriented to produce strong crystallographic texture within each secondary particle. Theoretical calculation showed that boron decreases the surface energy of the (003) planes, resulting in a preferential growth mode that maximizes the (003) facet. A key finding of this work is that microstructural optimization alone greatly improved the cycling stability of a Ni-rich NCA cathode, as the B-NCA88 cathode maintained 83% of its initial capacity after 1000 cycles even when it was cycled at 100% DOD. By contrast, the same cathode without boron retained only 49% of its initial capacity. The superior cycling stability clearly indicates the importance of the particle microstructure (i.e., the particle size, particle shape, and crystallographic orientation) in mitigating the abrupt internal strain caused by the phase transition in the deeply charged state, which occurs in all Ni-rich layered cathodes. Microstructure engineering by surface energy modification, when combined with protective coatings and modification of the composition, may provide a long-sought solution to harnessing the high capacity of Ni-rich layered cathodes without sacrificing the cycling stability.

Acknowledgements

This work was supported mainly by the Global Frontier R&D Programme (NRF-2013M3A6B1078875) at the Center for Hybrid Interface Materials (HIM) of the Ministry of Science, ICT & Future Planning. In addition, this work was also supported by a grant from Human Resources Development program (No. 20184010201720) of the Korea Institute of Energy Technology Evaluation and Planning (KETEP) funded by the Ministry of Trade, Industry and Energy of the Korean government. The work of Y.-S. Y. was supported by the Director, Office of Science, Office of Basic Energy Sciences, of the US Department of Energy (contract no. DE-AC02-05CH11231). This research used the resources of the Advanced Light Source, which is a DOE Office of the Science User Facility, under contract no. DEAC02-05CH11231.

Author contributions

Yang-Kook Sun: Supervision, Conceptualization, Writing - Review & Editing, Funding Acquisition; **Chong S. Yoon:** Conceptualization, Methodology, Writing - Review & Editing; **Payam Kaghazchi:** Conceptualization, Validation; **Hoon-Hee Ryu:** Investigation, Writing – Original Draft, Validation; **Nam-Yung Park:** Investigation, Validation; **Jeong Hyun Seo:**

Investigation; **Young-Sang Yu:** Investigation, Methodology, Software; **Monika Sharma:** Methodology, Investigation; **Robert Mücke:** Methodology, Investigation

Appendix A. Supplementary data

Supplementary data associated with this article can be found, in the online version.

References

[1] Ford R. Bryan, The Birth of Ford Motor Company, http://www.hfha.org, (accessed 20 November 2019).

[2] C. C. Chan, Proc. IEEE 101 (2013) 206−212.

[3] M. H. Westbrook, The Electric Car: development and future of battery, hybrid and fuel-cell cars, Institution of Engineering and Technology, Stevenage, 2001.

[4] D. Howell et al., in Energy Storage 2015 Annual Report, U.S. Department of Energy, Washington D.C., 2016, pp. 1−263.

[5] H.-J. Noh et al., J. Power Sources 233 (2013) 121–130.

[6] J.-H. Kim et al., ACS Appl. Mater. Interfaces 11 (2019) 30936−30942.

[7] H.-H. Ryu et al., Chem. Mater. 30 (2018) 1155−1163.

[8] C. S. Yoon et al., ACS Energy Lett. 2 (2017) 1150−1155.

[9] A. O. Kondrakov et al., J. Phys. Chem. C 121 (2017) 3286−3294.

[10] J.-M. Lim et al., Sci. Rep. 7 (2017) 39669.

[11] U.-H. Kim et al., Adv. Energy Mater. 9 (2019) 1803902.

[12] U.-H. Kim et al., Mater. Today 23 (2019) 26–36.

[13] S. Watanabe et al., J. Power Sources 260 (2014) 50–56.

[14] Y.-K. Sun et al., Nat. Mater. 8 (2009) 320–324.

[15] D.-W. Jun et al., Chem. Mater. 29 (2017) 5048–5052.

[16] P. Yan et al., Nat. Energy. 3 (2018) 600–605.

[17] K.-J. Park et al., Adv. Energy Mater. 8 (2018) 1801202.

[18] G. W. Nam et al., ACS Energy Lett. 4 (2019) 2995–3001.

[19] C. T. Rueden et al., BMC Bioinformatics 18 (2017) 529.

[20] S. Yamakawa et al., Solid State Ionics 319 (2018) 209–217.

[21] R. Xu et al., J. Electrochem. Soc. 164 (2017) A3333–A3341.

[22] D. A. Shapiro et al., Nat. Photonics 8 (2014) 765–769.

[23] D. A. Shapiro et al., Microsc. Microanal. 24 (2018) 8–10.

[24] J. Zhao et al., Proc. of SPIE 11112 (2019) 111120C.

[25] D. R. Luke, Inverse Probl. 21 (2004) 37–50.

[26] Y.-S. Yu et al., Nat. Commun. 9 (2018) 921.

[27] R. Mak et al., Faraday Discuss. 171 (2014) 357–371.

[28] V. F. Stewner et al., Acta Cryst. B27 (1971) 904–910.

[29] H.-H. Sun, A. Manthiram, Chem. Mater. 29 (2017) 8486–8493.

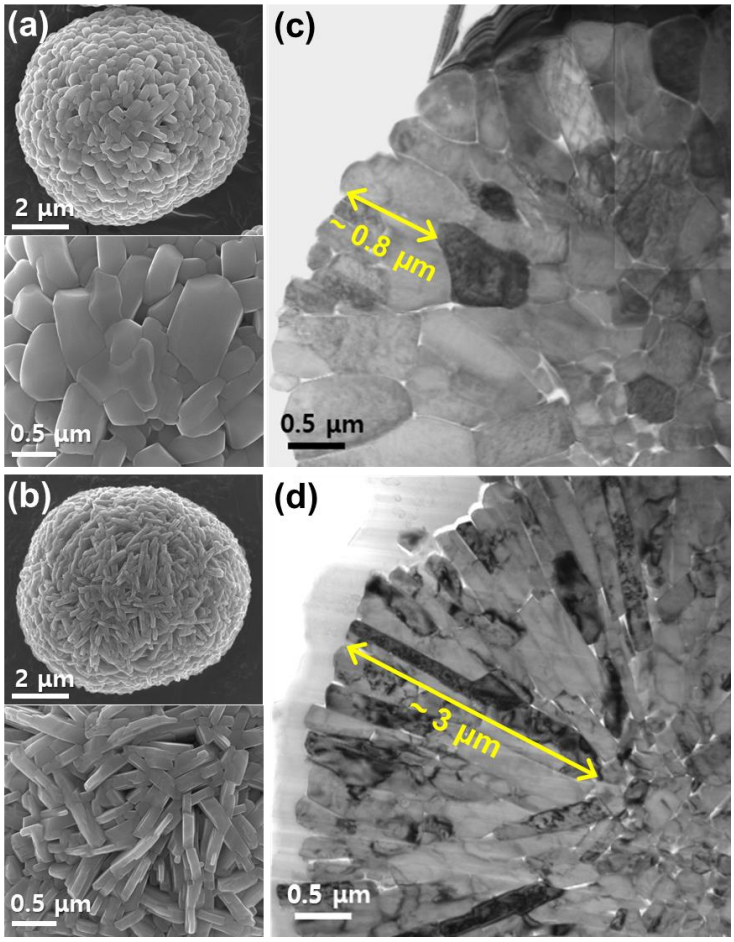

Fig. 1. SEM images of as-synthesized (a) P-NCA89 and (b) B-NCA88 cathode particles at different magnifications. Cross-sectional bright-field scanning TEM images of as-synthesized particles showing microstructure of (c) P-NCA89 and (d) B-NCA88.

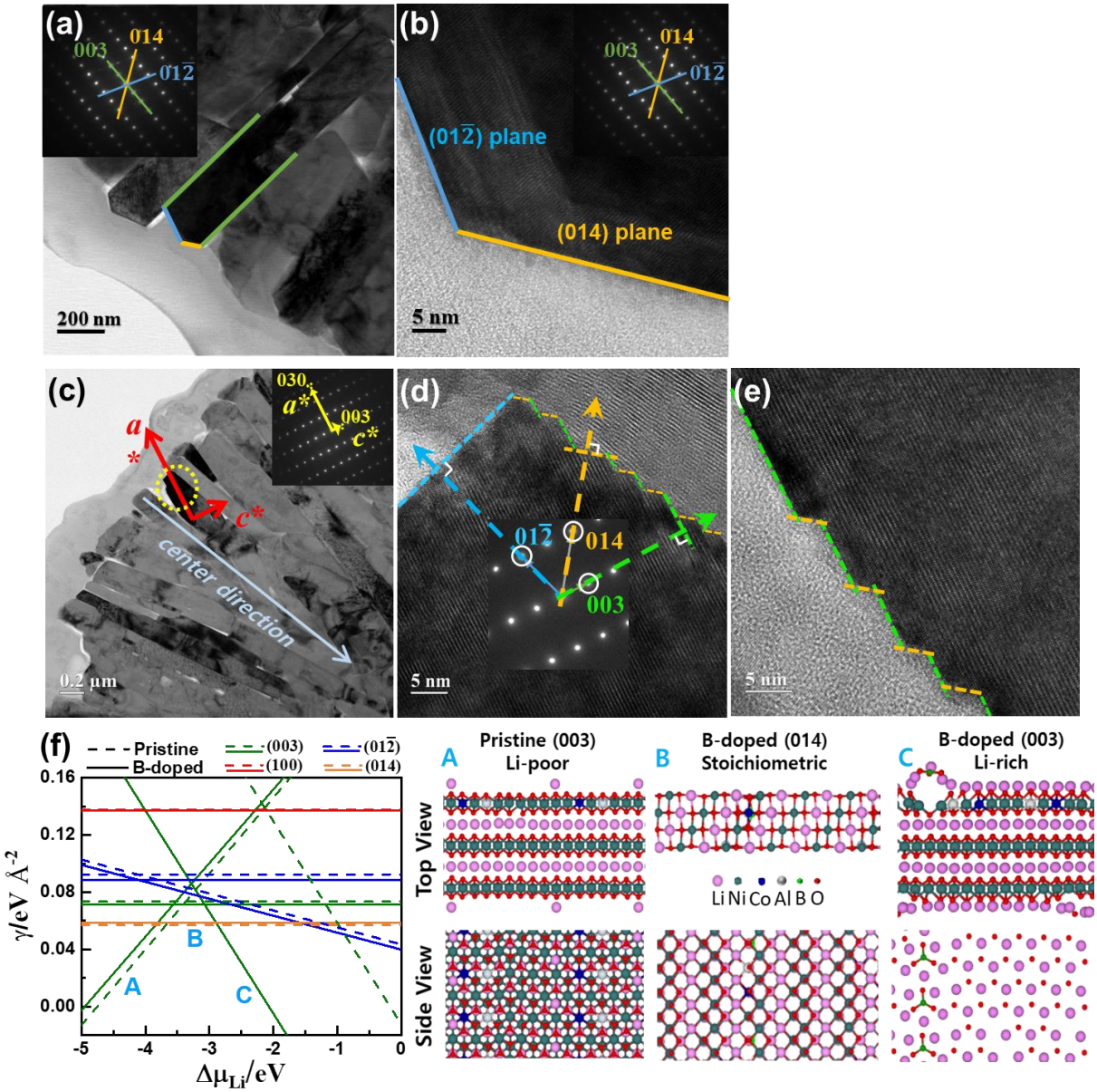

Fig. 2. (a,c) Bright-field TEM images of a primary particle of B-NCA88. High-resolution TEM images shown in (b) and (d,e) represent the magnified region of the marked primary particle in (a) and (c), respectively. Inset shows the selected-area electron diffraction pattern of the [100] zone. Green, blue, and orange lines indicate (003), (01$\bar{2}$), and (014) facets, respectively. (f) Surface energies of pristine and B-doped $LiNi_{0.9}Co_{0.04}Al_{0.04}O_2$ (003), (01$\bar{2}$), (100), and (104) surfaces as function of the chemical potential of Li ($\Delta\mu_{Li}$) referenced to bulk metal Li (left). Solid and dashed lines represent B-doped and pristine surfaces, respectively. Most favorable surface structures at different values of $\Delta\mu_{Li}$ (right), labeled as A: pristine (003)-Li poor, B: B-doped (014)-stoichiometric, and C: B-doped (003)-Li rich in the surface energy plot.

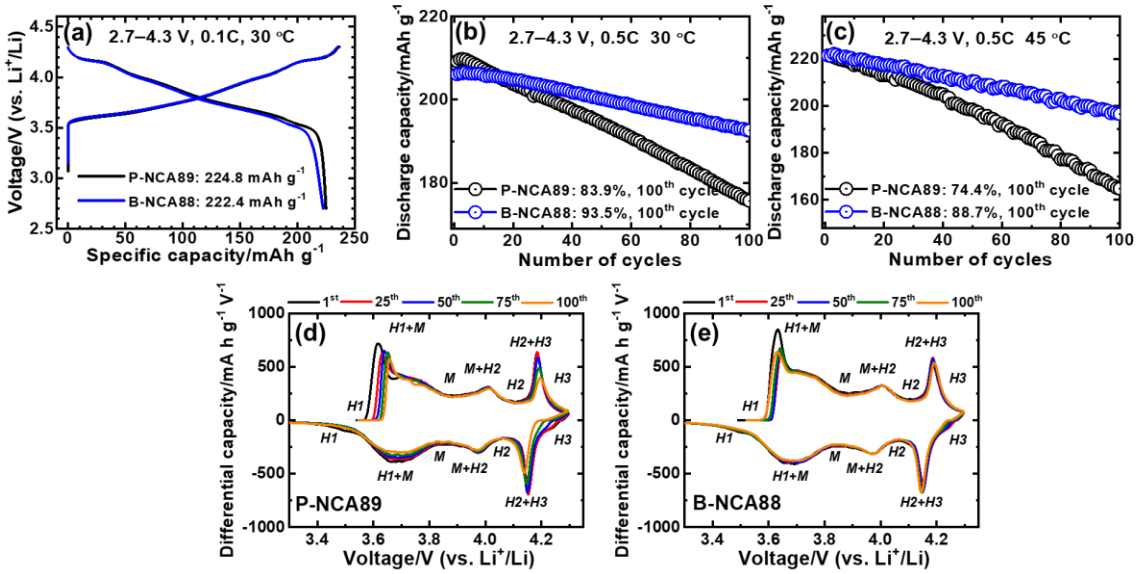

Fig. 3. Comparison of the electrochemical performance of P-NCA89 and B-NCA88: (a) initial charge–discharge curves at 0.1C and 30°C; cycling performance at 0.5C and (b) 30°C, (c) 45°C using 2032 coin-type half-cells with a Li metal anode. Differential capacity (d*Q*/d*V*) profiles as a function of the number of cycles for (d) P-NCA89 and (e) B-NCA88 cathodes.

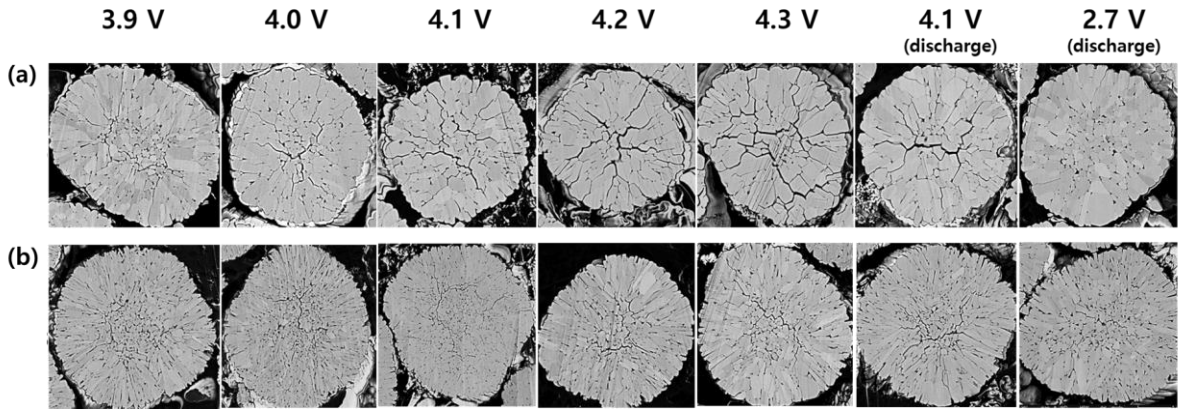

Fig. 4. Comparison of cross-sectional SEM images of (a) P-NCA89 and (b) B-NCA88 cathodes in various states of charge during initial cycle.

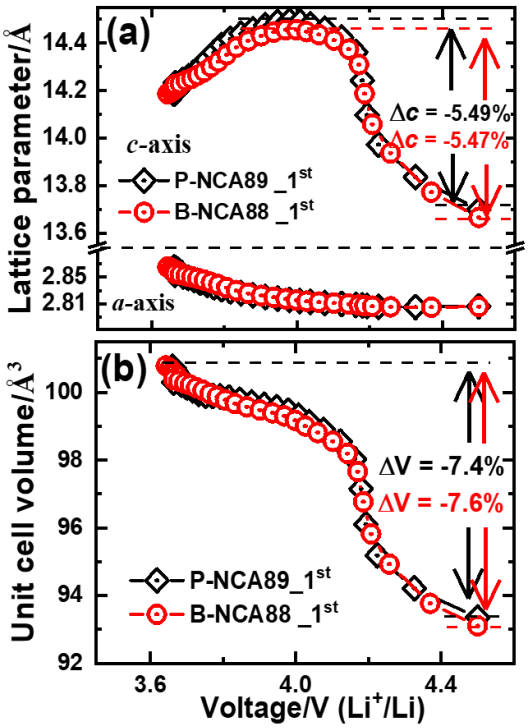

Fig. 5. Variation in (a) *a*-axis and *c*-axis lattice parameters and (b) unit cell volume as a function of voltage.

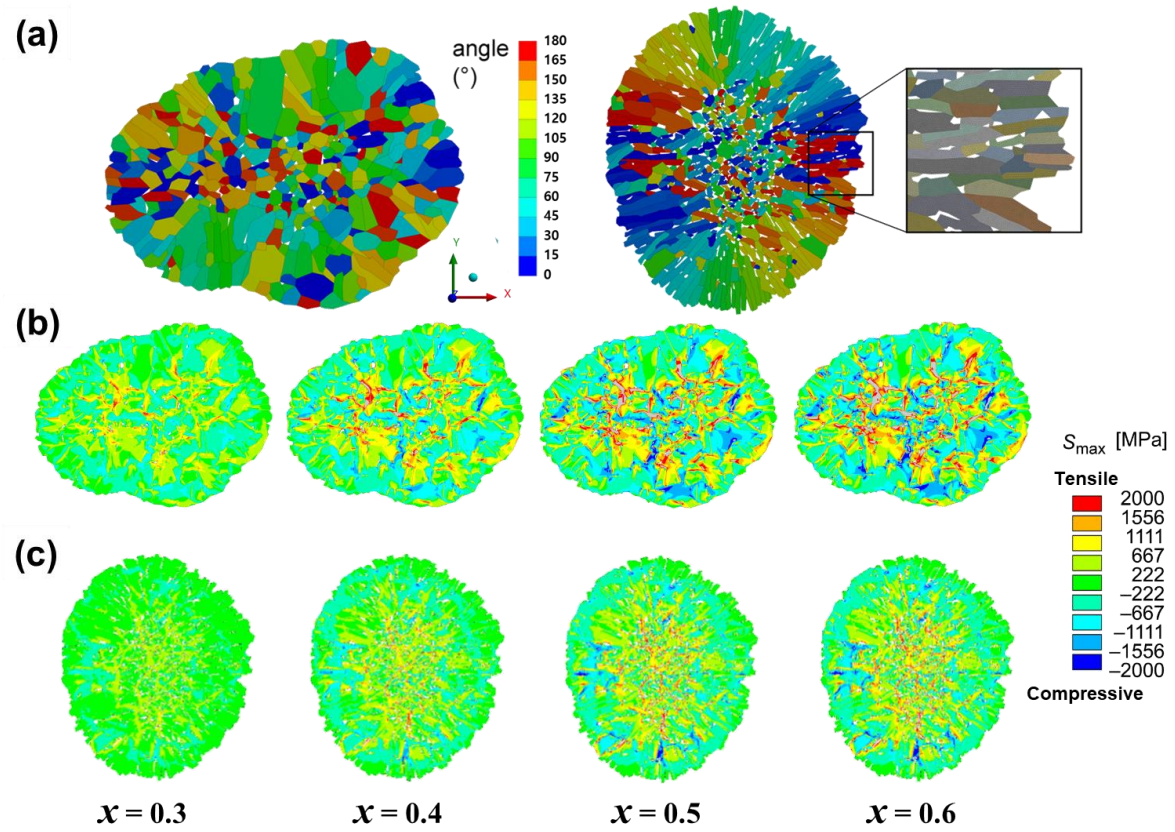

Fig. 6. Constructed microstructures and crystallographic orientation (angle between crystal *a* axis and *x* axis) of the (a) P-NCA-89 and B-NCA-88 particles based on TEM images and details about mesh and individual crystal colors. Calculated stress distribution (maximum principal stress) as a function of state of charge inside the (b) P-NCA89 and (c) B-NCA88 particles.

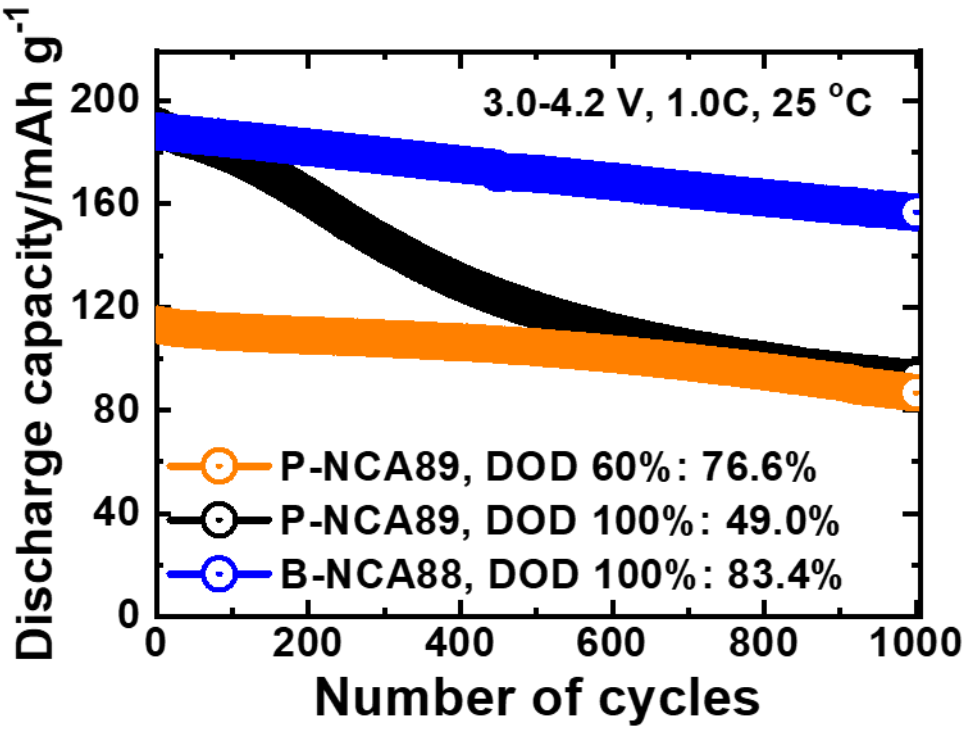

Fig. 7. Long-term cycling performance of P-NCA89 cathodes cycled at DOD 60% and 100%, and B-NCA88 cathode cycled at DOD 100%.

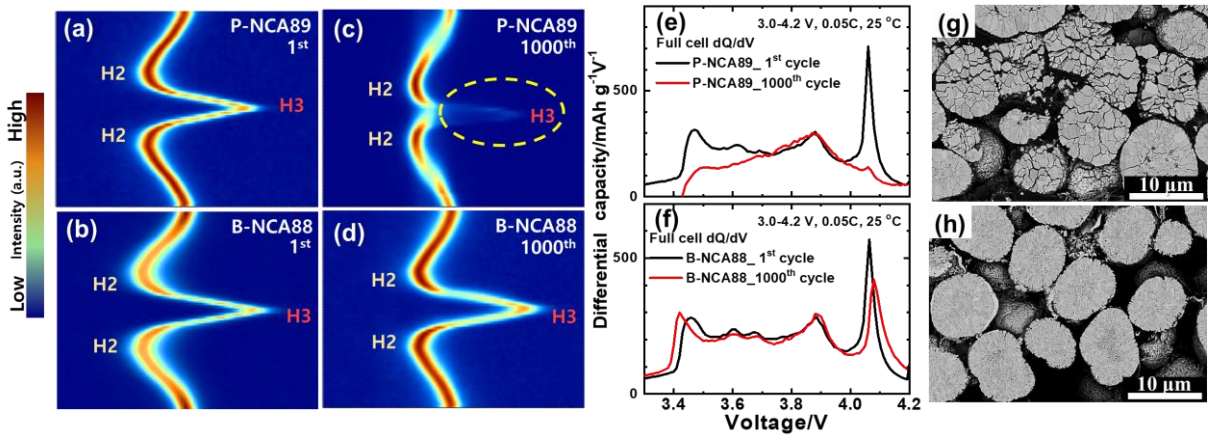

Fig. 8. Contour plots of (003) reflection of (a,c) P-NCA89 and (b,d) B-NCA88 measured at 1st and 1000th cycles, and (e,f) corresponding d*Q*/d*V* profiles. Cross-sectional SEM images after 1000 cycles for (g) P-NCA89 and (h) B-NCA88 cathodes.

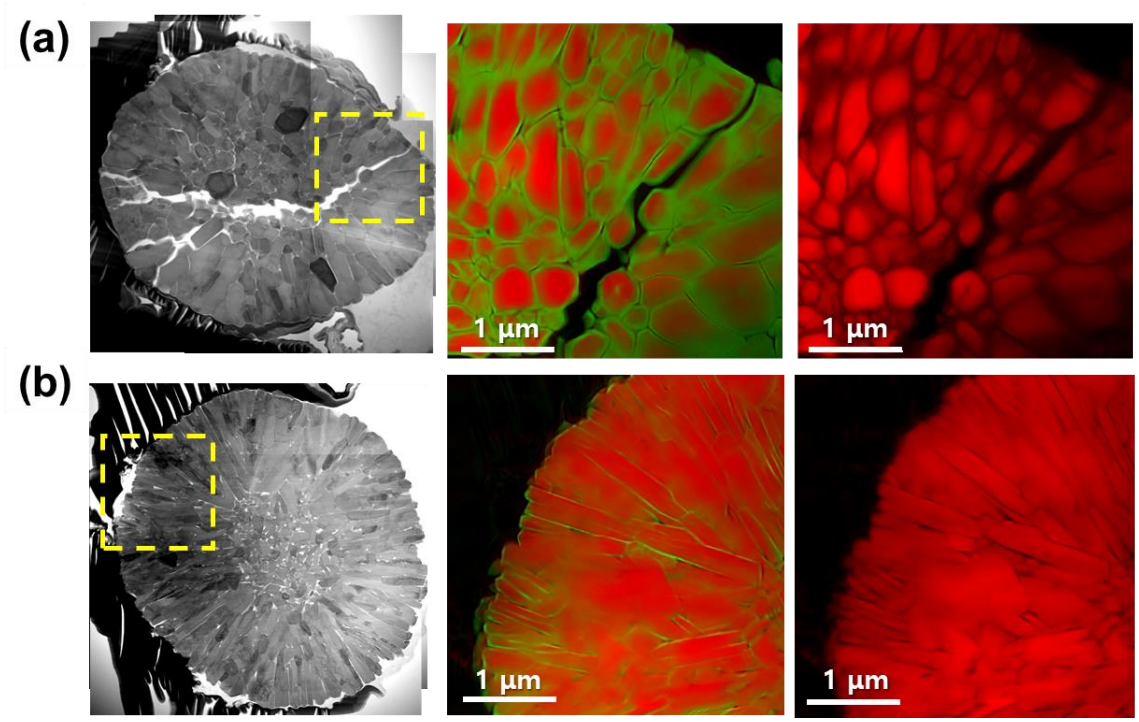

Fig. 9. Cross sections of the discharged (a) P-NCA89 and (b) B-NCA88 cathodes after 100 cycles and chemical maps of the marked regions obtained by ptychography. Chemical maps indicate both Ni^{2+} and Ni^{3+} (center) and only Ni^{3+} (right). Chemical phase maps were obtained assuming linear relationships between pixel-by-pixel XAS and reference spectra. The fitting results (chemical information) and averaged OD (morphological information) are indicated by color and transparency, respectively. Red and green represent Ni^{3+} and Ni^{2+}, respectively.

Supplementary data

A highly stabilized Ni-rich NCA cathode for high-energy lithium-ion batteries

Hoon-Hee Ryu[1], Nam-Yung Park[1], Jeong Hyun Seo[2], Young-Sang Yu[3], Monika Sharma[4], Robert Mücke[4], Payam Kaghazchi[4,*], Chong S. Yoon[2,*] Yang-Kook Sun[1,*]

[1]Department of Energy Engineering, Hanyang University, Seoul 04763, South Korea
[2]Department of Materials Science and Engineering, Hanyang University, Seoul 04763, South Korea
[3]Advanced Light Source, Lawrence Berkeley National Laboratory, Berkeley, CA 94720, USA
[4]Forschungszentrum Jülich GmbH, Institute of Energy and Climate Research, Materials Synthesis and Processing (IEK-1), 52425, Jülich, Germany

*** Corresponding authors.**
***E-mail addresses*: Kaghazchi, P. (payamk@zedat.fu-berlin.de) Yoon, C.S. (csyoon@hanyang.ac.kr), Sun, Y.-K. (yksun@hanyang.ac.kr)**

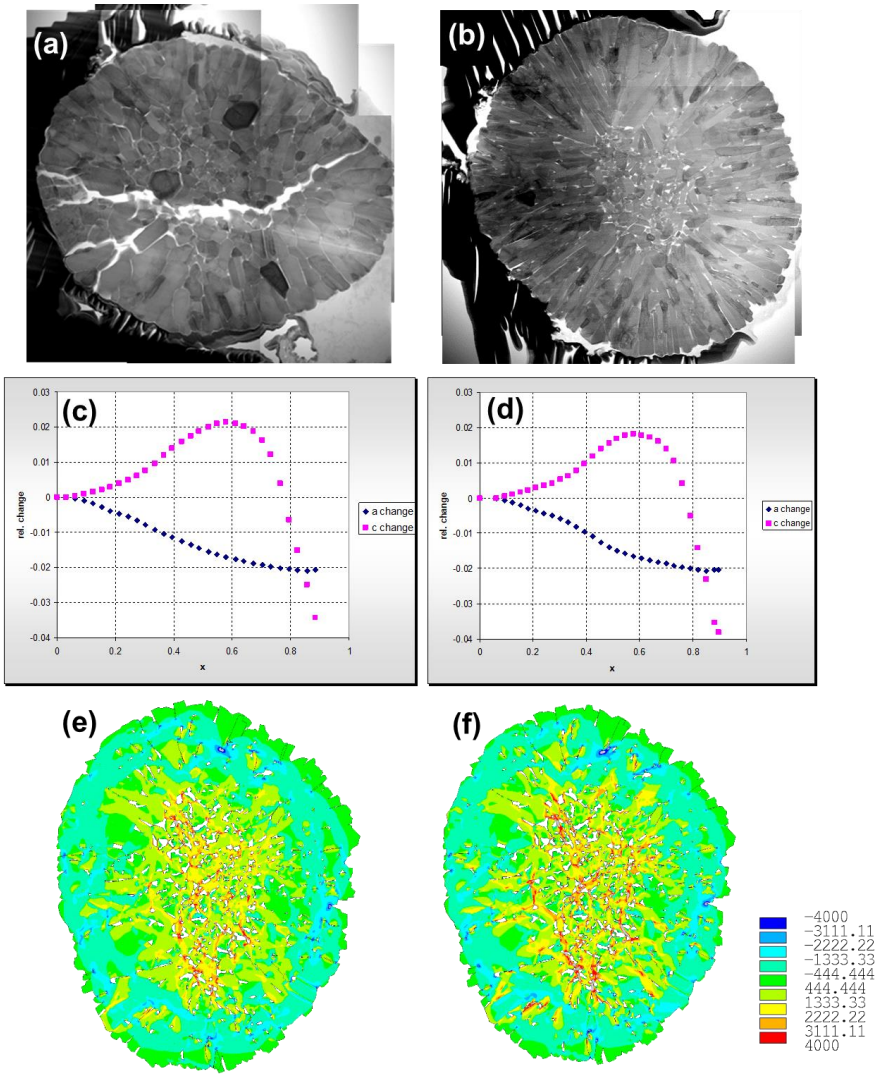

Fig. S1. Cross-sectional TEM image of (a) P-NCA89 and (b) B-NCA88. The particles in panel (a) and (b) are fully discharged state after 100 cycles using coin-type half-cells. Anisotropic lattice parameters change of (c) P-NCA-89 and (d) B-NCA-88 as function of the state of charge (*x*) measured by XRD. The change along the *b* axis equals the change along the *a* axis. Calculated stress distribution (maximum principal stress S_{max} in MPa) at x=0.6 in B-NCA-88 particle using (e) isotropic stiffness data of NMC532 reported by Xu et al [21]. and (f) anisotropic stiffness matrix of $Li_{0.5}CoO_2$ from Yamakawa et al [20].

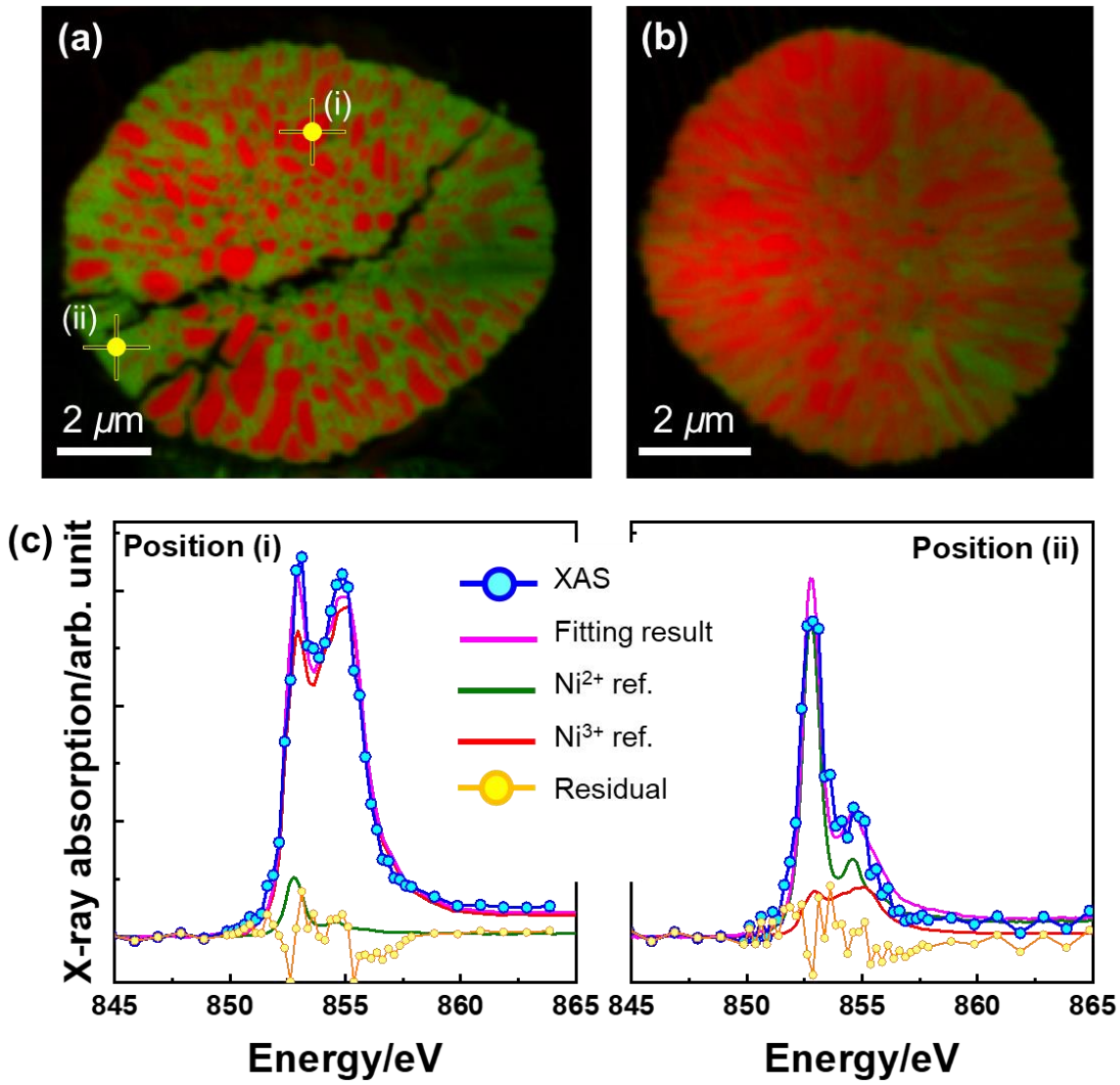

Fig. S2. Ni oxidation state maps obtained by LC fits of XAS data for the discharged (a) P-NCA89 and (b) B-NCA88 cathodes after 100 cycles using coin-type half-cells. Red and green indicate Ni^{3+} and Ni^{2+}, respectively. The transparency indicates the relative sample thickness along the X-ray path. (c) Selected single-pixel XAS spectra extracted at the marked positions in (a) and results of LC fits with standard spectra. The residual is defined as the difference between the XAS data and fitting results. The simulated concentrations of Ni^{2+} for pixels (i) and (ii) are 17.8% and 82.3%, respectively.

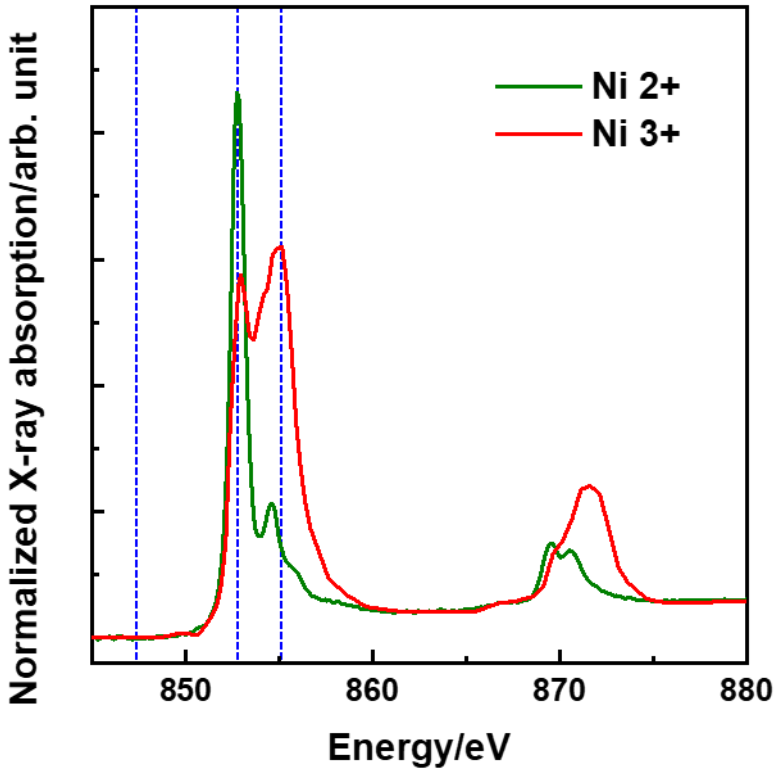

Fig. S3. Reference Ni *L*-edge X-ray absorption spectra of $LiMn_{1.5}Ni_{0.5}O_4$ (Ni^{2+}, green solid line) and $LiNi_{0.8}Co_{0.15}Al_{0.05}O_2$ (Ni^{3+}, red solid line). Ptychographic images were measured at the specific energies noted by blue dotted lines (847, 852.75, and 855 eV).

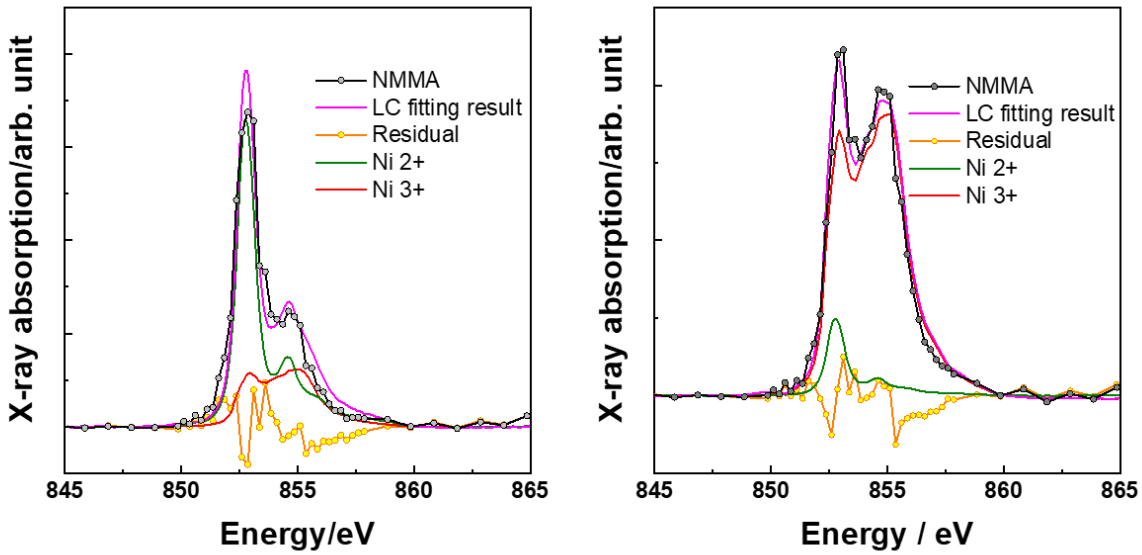

Fig. S4. Estimated end-member spectra of P-NCA89 obtained by non-negative matrix analysis. To justify the reference spectra, the calculated end-member spectra were simulated by LCs of reference spectra. The residual is defined as the difference between the end-member spectra and fitting results.

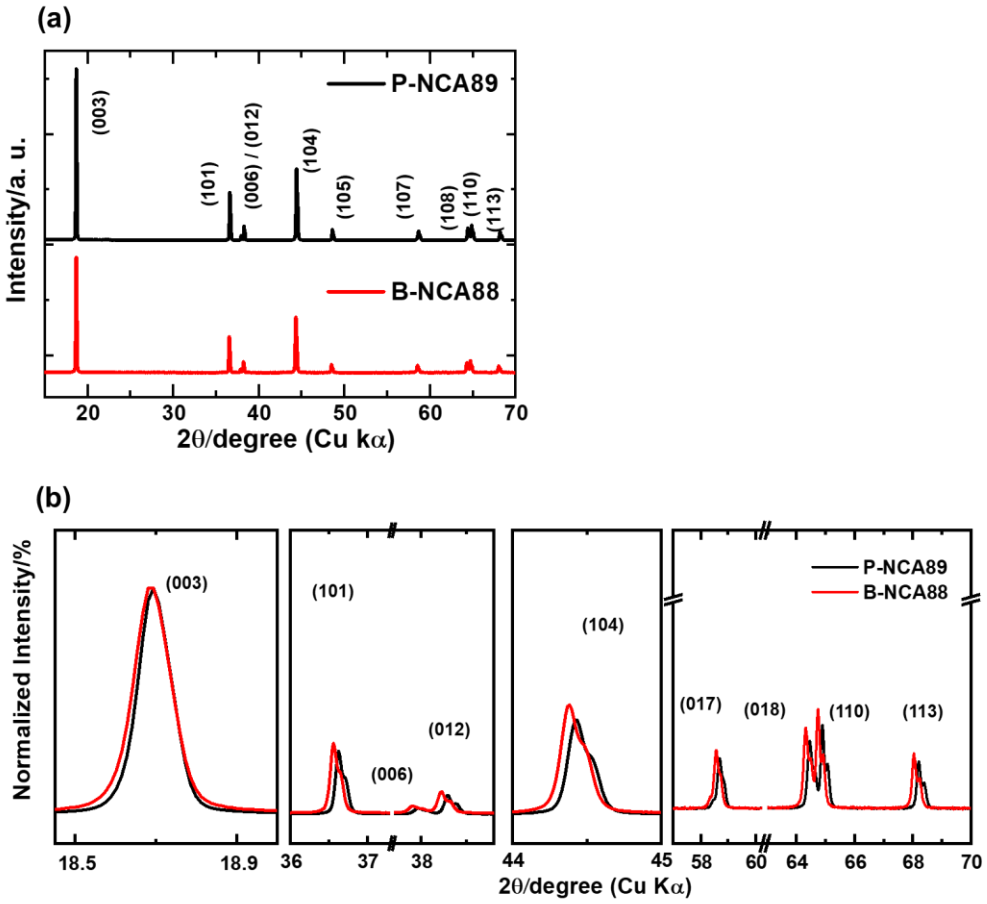

Fig. S5. (a) X-ray diffraction patterns of as-synthesized P-NCA89 and B-NCA88 cathodes and (b) magnified profiles after normalized by the intensity of (003) reflection in four different 2θ regions.

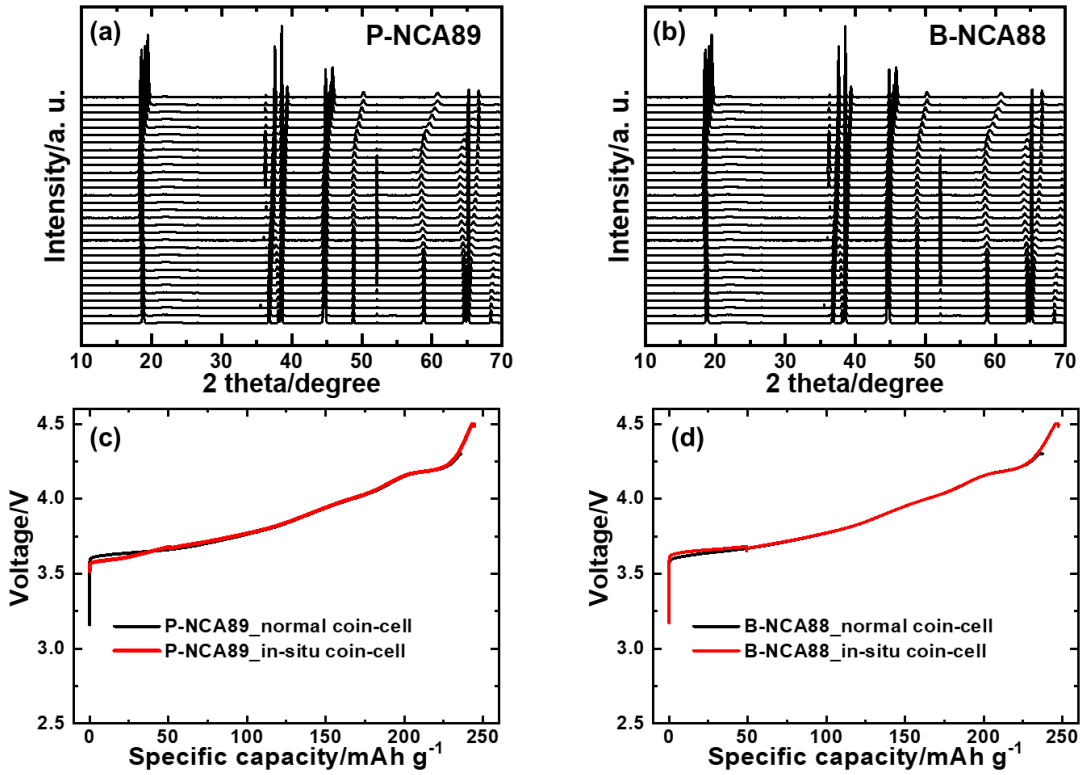

Fig. S6. The full XRD spectra are plotted during initial charge process for (a) P-NCA89 and (b) B-NCA88. Initial charge curves of (c) P-NCA89 and (d) B-NCA88 using normal and modified coin-type half-cells are plotted to guarantee the electrochemical reaction at a specific current of 40 mA g^{-1} during in-situ XRD measurement.

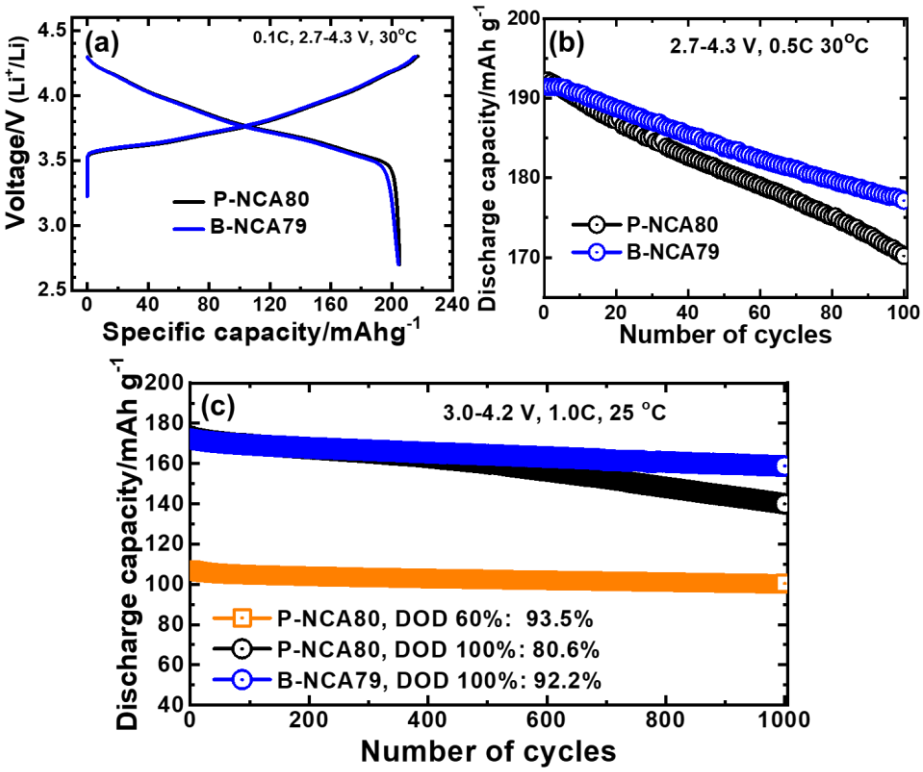

Fig. S7. Comparison of electrochemical performance of P-NCA80 and B-NCA79 using (a,b) coin-type half-cells for 100 cycles and (c) pouch-type full-cells for long-term cycling.

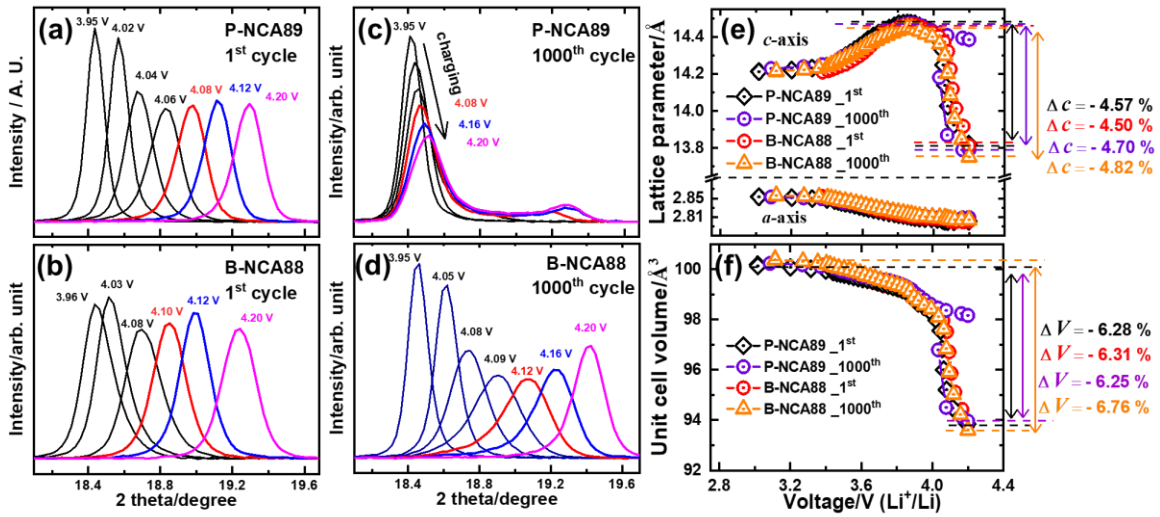

Fig. S8. In situ XRD patterns of the (003) reflection in selected voltage ranges during charging for (a,b) the 1st cycle and (c,d) the 1000th cycle, and (e,f) calculated lattice parameters for P-NCA89 and B-NCA88 cathodes.